RESEARCH

Solid-state electron-mediated z-scheme heterostructured semiconductor nanomaterials induce dual programmed cell death for melanoma therapy

Yiping Ren[1,2,3†], Yun Wang[4†], Cheng Chen[2,3], Xiang Yan[2,3], Minghao Chao[2], Yuting Li[2], Dehong Yu[2], Yuqi Huang[2,3], Xiaoyang Hou[3], Fenglei Gao[1,2*], Guan Jiang[3*] and Ming Guan[1*]

Abstract

The programmed cell death (PCD) pathway removes functionally insignificant, infection-prone, or potentially tumorigenic cells, underscoring its important role in maintaining the stability of the internal environment and warding off cancer and a host of other diseases. PCD includes various forms, such as apoptosis, copper death, iron death, and cellular pyroptosis. However, emerging solid-state electron-mediated Z-scheme heterostructured semiconductor nanomaterials with high electron-hole (e–h^+) separation as a new method for inducing PCD have not been well studied. We synthesize the Bi_2S_3-Bi_2O_3-Au-PEG nanorods (BB-A-P NRs) Z-scheme heterostructured semiconductor has a higher redox capacity and biocompatibility. Firstly, the BB-A-P NRs are excited by near-infrared (NIR) light, which mimics the action of catalase by supplying oxygen (O_2) and converting it to a single-linear state of oxygen ($^1O_2$) via e–h^+ transfer. Secondly, they react with hydrogen peroxide (H_2O_2) and water (H_2O) in tumor to produce hydroxyl radicals (•OH), inducing apoptosis. Intriguingly, the Caspase-1/Gasdermin D (GSDMD)-dependent conventional pyroptosis pathway induced cellular pyroptosis activated by apoptosis and reactive oxygen species (ROS) which causes the intense release of damage associated molecular patterns (DAMPs), leading to the inflammatory death of tumor cells. This, in turn, activates the immunological environment to achieve immunogenic cell death (ICD). BB-A-P enables computed tomography imaging, which allows for visualization of the treatment. BB-A-P activated dual PCD can be viewed as an effective mode of cell death that coordinates the intracellular environment, and the various pathways are interrelated and mutually reinforcing which shows promising therapeutic effects and provides a new strategy for eliminating anoxic tumors.

†Yiping Ren and Yun Wang contributed equally to this work.

*Correspondence:
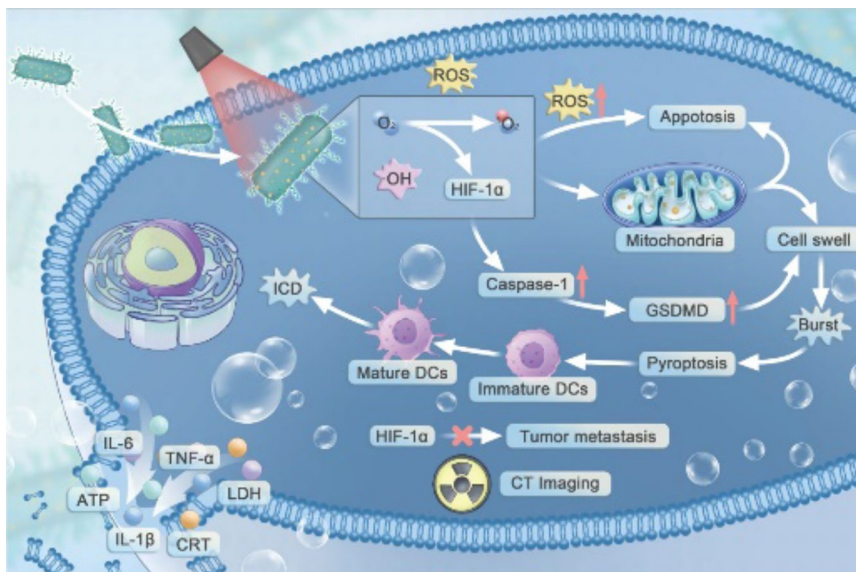Fenglei Gao
jsxzgfl@sina.com
Guan Jiang
guanming88@yahoo.com
Ming Guan
dr.guanjiang@gmail.com

Full list of author information is available at the end of the article

Graphical abstract

Introduction

Inducing PCD in tumors has long been a crucial approach in tumor therapy. ROS has been identified as one of the most significant factors in this field. The emergence of photocatalysts is a new approach to induce ROS production [1]. Light at specific wavelengths can excite various photosensitizers and nanomaterials to generate ROS for tumor destruction. Due to most of material have drawbacks, including poor water solubility, low biosafety, and poor biocompatibility, which limit their practical application [2]. Thus, in many studies of generating ROS for the treatment of diseases, unconventional photosensitizers have been used, including p-n junctions, type I and type II heterostructures, instead of conventional ones. Nevertheless, further exploration and challenges are necessary. Because of the complexation of that and the oxidation/reduction reaction on the surface of the photocatalyst is slowed down by charge separation and migration to the surface [3, 4]. Catalysts require higher valence band (VB) and conduction band (CB) levels from a catalytic perspective due to their sufficient redox potential [5]. Therefore, constructing heterojunctions is the most efficient and practical option. Solid-state electron-mediated Z-scheme heterojunctions offer more advantages than single catalysts, improving charge separation efficiency and promoting redox potential. This directly broadens the activity and range of catalytic reactions. All-solid-state Z-scheme heterojunctions have the potential to be highly effective in photonic therapeutics due to their high e^--h^+ pair separation efficiency and enhanced redox potential.

Bismuth is an extremely biocompatible transition metal with ultra-low toxicity, low price, and good tolerance even at high doses [6]. Bismuth has shown outstanding results in treating Helicobacter pylori infections, leading to the worldwide promotion of bismuth-related drugs [7–9]. Bi_2S_3-Bi_2O_3 (BB), with its e^--h^+ segregation, can be excited by NIR (808 nm) [10]. The wide band gap of Bi_2O_3 ensures total carrier concentration, resulting in a strong photocurrent response. The Z-scheme heterostructure formed by BB significantly improves photocatalytic efficiency. This is due to the matching of energy band positions between the broadly generated electrons in Bi_2O_3 and the photogenerated holes in Bi_2S_3 [11]. It is well-established that Au atoms can form strong bonds with sulfur (S) atoms [12]. Therefore, we conducted an insitu synthesis of gold nanoparticles (Au NPs) on the surface of Bi_2S_3-Bi_2O_3 nanorods (BB NRs) to create a new Z-Scheme System with solid state electron mediators. To enhance the overall biocompatibility of the nanomaterials, we coated the surface of the nanocomplexes with mercapto polyethylene glycol (mPEG-SH). Through NIR (808 nm) irradiation, h^+ on the VB of Bi_2S_3 and e^- on the CB of Bi_2O_3 migrate simultaneously to the intermediate conductor Au NPs, where they annihilate. This results in a more efficient separation of e^- on the CB of Bi_2S_3 and h^+ on the CB of Bi_2O_3, greatly reducing the probability of h^+ and e^- recombination. On the CB of Bi_2S_3, H_2O_2 is cleaved in the tumor microenvironment (TME)

Ren *et al. Journal of Nanobiotechnology*   (2024) 22:526

Page 3 of 18

to generate O_2 ($H_2O_2 + 4e^- \rightarrow 2H_2O + O_2 \uparrow$), which reduce the expression of hypoxia-inducible factor-1α (HIF-1α) in hypoxic environments. O_2 produces $^1O_2$ by gaining additional electrons. In Bi_2O_3's VB, h^+ can produce •OH by oxidizing H_2O and H_2O_2 in the TME [10, 11]. Au NPs and Bi_2S_3 are known to have high absorption efficiencies in the NIR region [13]. The excitation of NIR enhances the propensity of the synthesized BB-A-P NRs to produce electrons and holes in a simultaneous manner through thermal effects. This, in turn, affects their carrier mobility and compliance, thereby promoting ROS production [14]. Thus, activation of BB-A-P NRs by NIR can effectively alleviate the hypoxia of the TME, induce apoptosis of tumor cells, and achieve the goal of killing and inhibiting the metastasis of the tumor.

BB-A-P NRs are both safe and highly effective. They can efficiently induce apoptosis in tumor cells through the generation of O_2 and ROS. The cytotoxicity of ROS is mainly realized by oxidative stress. When the level of ROS is increased to a certain degree, it can activate apoptosis-related proteins, disrupt the mitochondrial membrane potential, and then induce apoptosis [15]. Additionally, ROS and apoptosis can cause tumor cells to undergo other form of PCD known as cellular pyroptosis. Many types of proteins have made new breakthroughs in the field of tumor therapy, such as cytokines, and pyroptosis substrates (Gasdermin family), have been discovered for tumor therapy [16–19]. Cellular pyroptosis is a PCD modality that promotes inflammation, and GSDMD proteins play a key role in the pathway, [19, 20] and involving both a variety of cysteine-aspartate proteases, notably Caspase-1, 4, 5, and 11 [21]. Surprisingly, caspase-induced apoptosis can be transformed into cellular pyroptosis through the expression of GSDMD [22]. Cellular pyroptosis involves cell swelling and fragmentation, resulting in the release of cellular contents that trigger intense inflammation [23]. The production of ROS can stimulate changes in the mitochondrial modal potential, this irreversible change that can induce apoptosis, meanwhile, it can also produce mitochondrial toxins that can reverse the oligomerization of the GSDMD and increase the expression content of the GSDMD furtherly leads to pyroptosis of tumor cells through the Caspase-1/GSDMD pathway. Caspase-1 cleaves GSDMD to GSDMD-N, which targets the cell membrane, disrupting intracellular osmotic pressure and inducing penetration. This leads to the release of cellular contents, such as lactic dehydrogenase (LDH), causing inflammatory death of tumor cells. This generates a chain reaction that can spread. Simultaneously, broken cells induce a reversal in the release of cellular contents, leading to a massive release of DAMPs such as surface-exposed calreticulin (CRT), adenosine triphosphate (ATP), and interleukin-1β (IL-1β). These molecules remodel the TME, which will increase the maturation of dendritic cells (DCs), further promote the presentation of T cells, activate the immune response and produce long-term immune effects, reverse its immunosuppressive state and induce ICD.

Visualization of treatment is a significant aspect of tumor therapy. Fortunately, BB-A-P can be used as a diagnostic nanomedicine to assist in computed tomography (CT) imaging for precise cancer diagnosis due to the high atomic number of bismuth (Z=83). The BB-A-P NRs are synthesized meticulously and are emerging photosensitizers. They improve the hypoxic tumor microenvironment and utilize the substrates in the environment to generate multiple ROS (•OH, $^1O_2$) and contrast agents for CT, activate the Caspase-1/GSDMD pathway, mutual promotion with the apoptosis pathway to achieve dual PCD of tumor cells, improve the immune environment within the tumor, and induce "explosive" death of tumor cells. We have synthesized an inexpensive and biologically safe semiconductor "photosensitizer" for tumor therapy by designing and customizing semiconductor heterostructures, which provides a new idea for tumor therapy.

Materials and methods

The synthesis of Bi2S3-Bi2O3-Au-PEG composite1

Take 50 mg of synthesized Bi_2S_3-Bi_2O_3 nanorods dispersed with deionized water, add 16.5 μL of tetrachloroauric acid (HAuCl$_4$) solution (1 g/mL), and stir magnetically under the condition of avoiding light for 4 h. Then, 600 μL of 100 mM sodium borohydride solution (NaBH$_4$) was added and stirred for 2 h. After the obtained mixed solution was washed several times, the precipitate was dried at 60 ℃ overnight. The precipitates were then dried in an oven at 60℃ overnight, and the black powder was obtained as Bi_2S_3-Bi_2O_3-Au nanorods. Bi_2S_3-Bi_2O_3-Au was obtained by taking 10 mg of dried Bi_2S_3-Bi_2O_3-Au dissolved in deionized water, adding 40 mg of mercapto polyethylene glycol (mPEG-SH), and magnetic stirring at room temperature for 24 h.(Scheme 1)

Cell uptake experiments

The cellular uptake capacity of BB-A-P NRs was determined by Confocal laser scanning microscope (CLSM). BB-A-P (20 μg/mL, PBS) and FITC were agitated at 4 °C under light protection for 24 h. B16F10 cells (2×10^5) were evenly distributed in confocal dishes, and after the cells adhered to the wall, they were co-incubated with BB-A-P NRs coupled with FITC in a 37 °C incubator for different time periods (0. 5, 2, 4, and 6 h), and were gently rinsed with PBS for 2 times, and then stained with DAPI for 10 min, rinsed again with PBS for 2 times, rinsed the fluorescent dye clean, firstly observed the green fluorescence intensity by CLSM, and secondly examined the fluorescence results by flow cytometer to the fluorescence
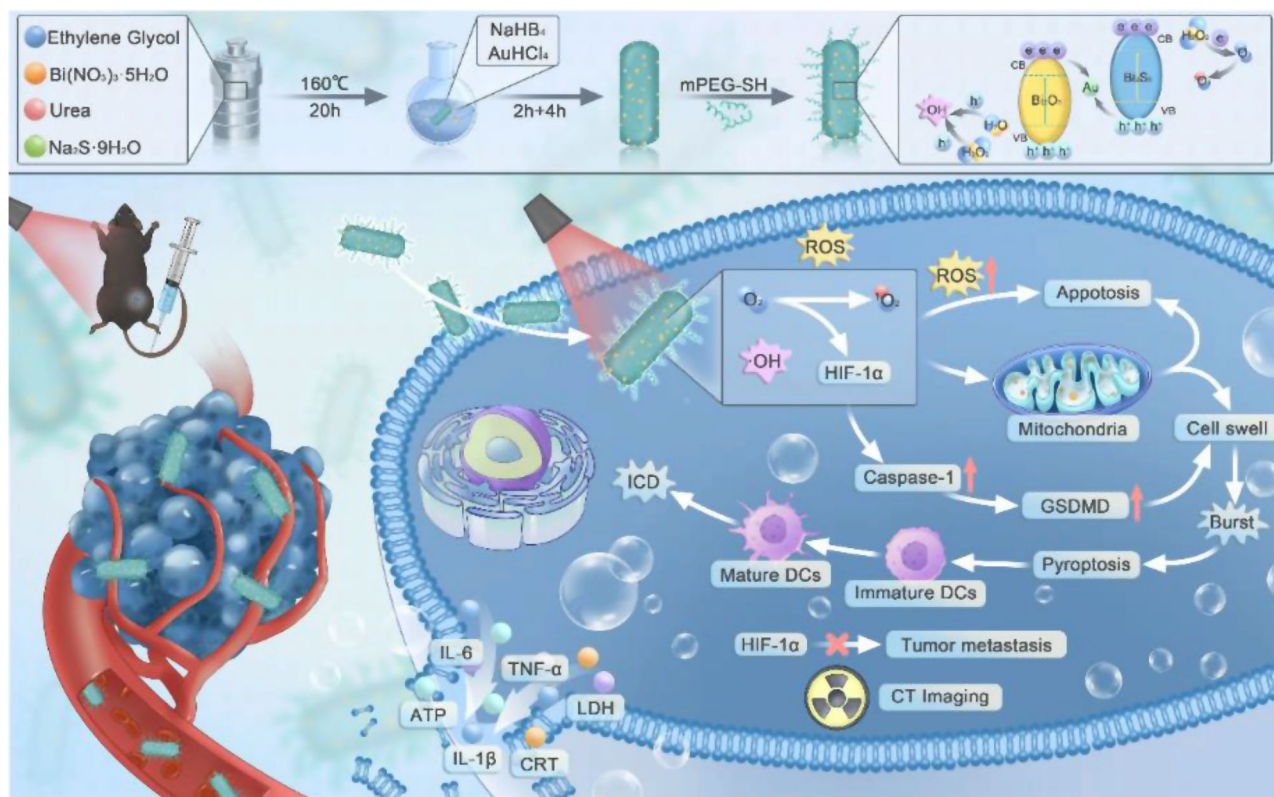
Scheme. 1 Schematic illustration of the fabrication and mechanism to induce pyroptosis of BB-A-P nanoparticles for cancer immunotherapy

results were firstly observed by CLSM and secondly examined by flow cytometer.

Characterization of BB-A-P NRs

The morphology of the nanomaterials was observed by transmission electron microscopy (TEM; Tecnai G2 Spirit Twin, FEI). The valence states of the components of the BB-A-P nanoplatform were analyzed by X-ray photoelectron spectroscopy (XPS) (ESCALAB 250). Fourier transform infrared (FTIR) spectra were obtained using an FT-IR spectrometer (IRAffinity-1s, SHIMADZU). Zeta potential and DLS of various samples were measured using Brookhaven instruments. Bio-Rad 680 zymography was used to detect the characteristic absorption of MB in the zymography plates and CCK-8 method, among others. Observations were made using a fluorescence inverted microscope (IX73P1F, Olympus, Japan) and a laser scanning confocal microscope (FV10i, Olympus, Japan). Laser treatment was performed using an 808 nm near-infrared laser (2.0 W/cm^2) (Beijing Leizhiwei Optoelectronic Technology Co., Ltd.). Laser confocal microscope (Leica STELLARIS 5, Germany) was used to take CLSM pictures. Flow cytometry analysis was performed using a flow cytometer (FACS Canto II, NULL). In vivo fluorescence imaging was performed using the IVIS imaging system (Lumina-II, Caliper Life Sciences, USA).

Generation of BB-A-P NRs

The production of O_2 in deionized water was measured using a dissolved oxygen meter. The experiment consisted of three groups: H_2O_2+NIR group, BB+H_2O_2+NIR group, and BB-A-P+H_2O_2+NIR group. In each group, 1 mg of BB-A-P NRs or BB NRs was dissolved in 10 mL of deionized water with H_2O_2 (20 mM). The solution was then irradiated with NIR (808 nm, 1.0 W/cm^2), and the dissolved oxygen level was recorded every 5 min using a dissolved oxygen meter. The experiment was repeated three times under the same conditions.

ROS generation of BB-A-P NRs

To assess the ability of BB-A-P NRs to generate ROS extracellularly, we dissolved 200 μg of BB-A-P NRs in a solution of MB (10 mg/L) and recorded the absorbance changes of MB at 664 nm at 0, 2, 4, 8, and 10 min under NIR (808 nm, 1.0 W/cm^2) irradiation. We detected $^1O_2$ generation in deionized water using TEMP and SOSG fluorescent probes and DPBF. To test the ability of BB-A-P NRs to produce extracellular •OH, we mixed different concentrations of BB-A-P (20, 50, 80, 100, and 120 μg/mL) with H_2O_2 (5 mM). Then, after NIR (808 nm, 1.0 W/cm^2) irradiation, we monitored the absorbance of TMB at 652 nm by scanning the UV-Vis-NIR spectra of the samples. Additionally, we detected the generation of different subgroups of •OH using DMPO. It was categorized into

the NIR (808 nm, 1.0 W/cm^2) group, NIR+H_2O_2 (5 mM) group, BB-A-P (100 μg/mL) group, BBAP+NIR group, BBAP+H_2O_2 group, and BB-A-P+H_2O_2+NIR group.

Cell culture

B16F10 and L929 cells were cultured in high-sugar DMEM (supplemented with 10% FBS), and all cells were incubated at 37 °C in 5% CO_2.

In vitro generation of O2

To detect the O_2 production of BB-A-P NRs in cells, B16F10 cells were inoculated into confocal dishes and a hypoxic cell incubator until the cells adhered to the wall. The experiments were performed in groups by setting up control group, H_2O_2 group, BB-A-P (20 μg/mL) group, and BB-A-P+NIR (50 μg/mL, 808 nm, 1.2 W/cm^2, 5 min) group. Then, incubation with [Ru(dpp)$_3$] Cl$_2$ was continued for 2 h in an anoxic cell incubator, and the fluorescent probe in the culture dish was washed with PBS, and the fluorescence intensity was observed under CLSM. The cell attachment step was repeated; the cells were fixed with 4% paraformaldehyde, permeabilized with 0.1% Trition-100 permeabilized B16F10 cells, labeled the B16F10 cells with HIF-1α antibody at a diluted concentration of 1:00, incubated the cells overnight at 4 °C on a shaker and protected from light, and then washed the dishes with PBS, incubated with goat anti-rabbit IgG antibody (1: 200) for 2 h, incubated with PBS, was gently rinsed 3 times for 5 min each, and finally stained with DAPI for 10 min, and the fluorescence intensity was observed under CLSM. The concentration of the HIF-1α antibody was adjusted to 1:500, and Western blot experiments were performed under the same conditions.

In vitro generation of ROS

The level of intracellular ROS production was detected using DCFH-DA. The experiments were divided into control, BB-A-P (20 μg/mL), BB-A-P+H_2O_2 (100 μM), and BB-A-P+H_2O_2+NIR (808 nm, 1.2 W/cm^2, 5 min) groups, and B16F10 cells were treated for 6 h according to the different subgroups. B16F10 cells were co-incubated with DCFH-DA dissolved in serum-free high-glucose DMEM medium and incubated for 40 min, and the intensity of green fluorescence was observed under an inverted microscope. After the cells were treated in the same way and co-incubated with DCFH-DA, the fluorescence expression was detected by a flow cytometer.

Biocompatibility assay

To test the cell safety of BB-A-P NRs, the CCK-8 method was used for the experiments. The experiments were grouped according to different concentrations (5, 10, 20, 50, 80, 120 μg/mL), and B16F10 and L929 cells were cultured in 96-well plates. After the cells were completely attached to the wall, the medium was aspirated, and 200 μL of serum-free medium with the corresponding concentration of nanorods was added to the corresponding experimental wells, and the cells were incubated for 24 h. The sample absorbance was detected at 450 nm under the microplate reader, and the experiment was repeated three times under the same conditions.

In vitro apoptosis assay

Apoptosis was detected by mitochondrial membrane potential, live/dead assay and apoptosis kit, respectively. B16F10 cells were inoculated into 12-well plates, and different treatments were performed after the cells were attached to the wall: control group, H_2O_2 (100 μM)+NIR (808 nm, 1.2 W/cm^2, 5 min) group, BB-A-P (20 μg/mL) group, BB-A-P+NIR group, BB-A-P+H_2O_2 group, BB-A-P+H_2O_2+NIR group, and a total of 8 h were incubated, after which the cells were incubated with serum-free medium containing JC-1 staining solution for 1 h, and then washed 3 times with PBS to clean the involved staining solution, and DAPI was added to stain the nuclei for 10 min, and then observed by inverted microscope and detected by flow cytometer with the same treated cells. In the same grouping as above, live and dead cells were stained with fluorescein calcium (AM) and propidium iodide (PI) and observed under an inverted microscope. In addition, apoptosis was detected by flow cytometry. Same treatment as above, then cells were separated by trypsin without ethylenediaminetetraacetic acid (EDTA), washed 3 times with PBS, then cells were treated with Annexin V-FITC Apoptosis Analysis Kit, and apoptosis was detected by flow cytometry after filtering cells with a cell sieve.

In vitro cellular pyroptosis

To detect focal cell death, we chose to observe the cell morphology under the inverted microscope, immunofluorescence detection, enzyme-linked immunosorbent assay (ELISA), and Western blot experiments for verification. The experiments were divided into the control group, BB-A-P (20 μg/mL) group, BB-A-P+H_2O_2 (100 μM) group, and BB-A-P+H_2O_2+NIR (1.2 W/cm^2, 5 min) group. B16F10 cells were inoculated into 12-well plates, and after 8 h of the corresponding treatments, the cells were irradiated with NIR for 5 min and then further cultured in the incubator for 6 h and finally the cell morphology was observed under an inverted microscope. Using the same treatment, BB-A-P+NIR group was added, and immunofluorescence staining was performed with Caspase-1 antibody and CRT, washed three times with PBS, and the nuclei of the cells were stained by adding DAPI dye for 10 min, and then the fluorescence expression was observed under CLSM. Cells were treated in the same way, labeled with Caspase-1 and GSDMD-N antibodies,

cells were lysed, proteins were extracted for Western-blot experiments, protein expression was observed, repeated 3 times, and Image J was used for quantitative analysis. Elisa experiments were performed after treatment using different groups of cell supernatants.

Tumor model

All experimental protocols were approved by the Ethics Committee of Xuzhou Medical University (202306T020, Xuzhou Medical University, Xuzhou, China). Five-week-old female C57BL/6X mice were used. B16F10 cells (2×10^6 B16F10 cells dissolved in 100 μL PBS) were injected subcutaneously into the right hind limb region of each mouse to establish a mouse model.

In vivo treatment evaluation

The experimental mice were divided into 4 groups (*n*=5): control group, NIR (808 nm, 1.2 W/cm², 10 min) group, BB-A-P (5 mg/kg) group, BB-A-P+NIR group. The body weight of the mice and tumor volume were recorded every other day to evaluate the treatment effect. The volume of tumors was measured every other day by caliper, and the formula was: tumor volume= (tumor length) × (tumor width)²/2. Blood, tumor and major organs after different treatments were collected for blood index test and H&E staining and HIF-1α, Caspase-1, CRT, Tunel, and Ki-67 staining to evaluate the therapeutic effect.

In vivo CT imaging

BB-A-P NRs were injected into tumors of hormonal mice at 2 mg/mL PBS solution (100 μl), and CT scans were performed 2 h postinjection.

Statistical analysis

Data in the text are presented as mean±standard deviation, and all experimental results were subjected to at least three independent experiments. Unpaired Student's two-tailed t-test was used to analyze statistical differences between the two groups. One-way ANOVA and post hoc tests (Dunnett's test) were used to analyze statistical differences between more than three groups of data. GraphPad Prism (GraphPad Software Inc.) was used for statistical analysis. Statistical differences were defined as follows: *P<0.05, **P<0.01, ***P<0.001, ****P<0.0001, n.s., not significant.

Results and discussion

Characterizations of BB-A-P NRs

The BB-A NRs were synthesized using simple hydrothermal and in situ reduction methods, among others, with improvements made to the previous synthesis method [24]. We observed the morphology of BB-A nanorods by transmission electron microscopy (TEM) (Fig. 1a). The elemental composition was determined through elemental mappings (Fig. 1b) and energy-dispersive X-ray spectroscopy (EDS) mapping, with Bi (26.5%), O (5.1%), S (7.4%), and Au (12.1%) uniformly distributed throughout the BB-A NRs (Fig. 1c). Using high-resolution transmission electron microscopy (HRTEM) images, we observed the coexistence of Bi_2O_3 and Bi_2S_3 phases and their compositions (Fig. 1d). X-ray photoelectron spectroscopy (XPS) analysis of the synthesized BB-A NRs revealed five major peaks representing O 1 S, C 1 S, S 2P, Bi 4f, and Au 4f (Fig. 1e). The binding energies of the peaks of Bi_2O_3 at 163.5 eV and 158.2 eV show spin-orbit splitting signals of Bi $4f_{7/2}$ and Bi $4f_{5/2}$, indicating that Bi exists in the oxidized state Bi^{3+} (Fig. 1f). The doping of Bi_2S_3 alters Bi_2O_3. The two Bi 4f bands may also be split into two groups of peaks, with the first group located at 163.5 and 158.2 eV with 5.3 eV in between, belonging to the Bi^{3+} species (Bi $4f_{5/2}$ and Bi $4f_{7/2}$) of Bi_2O_3. The fragment describes the binding energy of the Bi^{3+} species of Bi_2S_3. Two characteristic peaks are observed near 162.5 eV and 163.5 eV, which belong to S $2p_{3/2}$ and S $2p_{1/2}$, respectively (Fig. 1g). The synthesis of Bi_2S_3 was successfully demonstrated. In situ reduction was used to attach Au nanoparticles to the surface of Bi_2S_3-Bi_2O_3 NRs by utilizing the defective sites of Bi_2S_3, the peaks located around 161.5 eV (Fig. 1g). Additionally, the high-resolution spectra of the O 1s regions for BB, with major peaks located around 529.5 eV (Fig. 1h). The high-resolution Au XPS spectrum shows two peaks of Au at 82.8 and 86.8 eV, corresponding to metallic Au $4f_{7/2}$ and $4f_{5/2}$, respectively (Fig. 1i). The Bi 4f displacement indicates an electronic interaction between Bi_2S_3 and Bi_2O_3 at their interface, suggesting the formation of a BB-A heterostructure (Fig. 1j). The BB phases were characterized by XRD (Fig. 1k), and their diffraction peaks matched with the joint committee on powder diffraction standards (JCPDS) card No. 17–0320 and the JCPDS card No. 41-1149 corresponding to Bi_2S_3 and Bi_2O_3 phases, respectively. This indicates that the hydrothermal method successfully synthesized BB NRs [25]. To achieve good biocompatibility, the surface of Bi_2S_3-Bi_2O_3-Au NRs was modified by coupling mPEG-SH through Bi-S or Au-S bonds [26]. The success of the modification was confirmed by zeta potential and Fourier transform infrared (FTIR) spectroscopic measurements. It was demonstrated by the experimental results that the surfaces of BB-A-P effectively encapsulated mPEG-SH. The zeta (*ζ*)-potential was measured after envelopment with mPEG-SH, and the average value changed from 14.3 mV before wrapping to -19.6 mV (Figure S1). The Fourier analysis results showed that in BB-A-P, the characteristic peak of Bi_2S_3 at 1104 cm⁻¹ and the peaks near 844 cm⁻¹ and 530 cm⁻¹ may be the superposition of Bi-O stretching vibration over C-S stretching vibration, indicating that physical adsorption had occurred [27, 28]. The study demonstrated that the mPEG *ζ*-potential
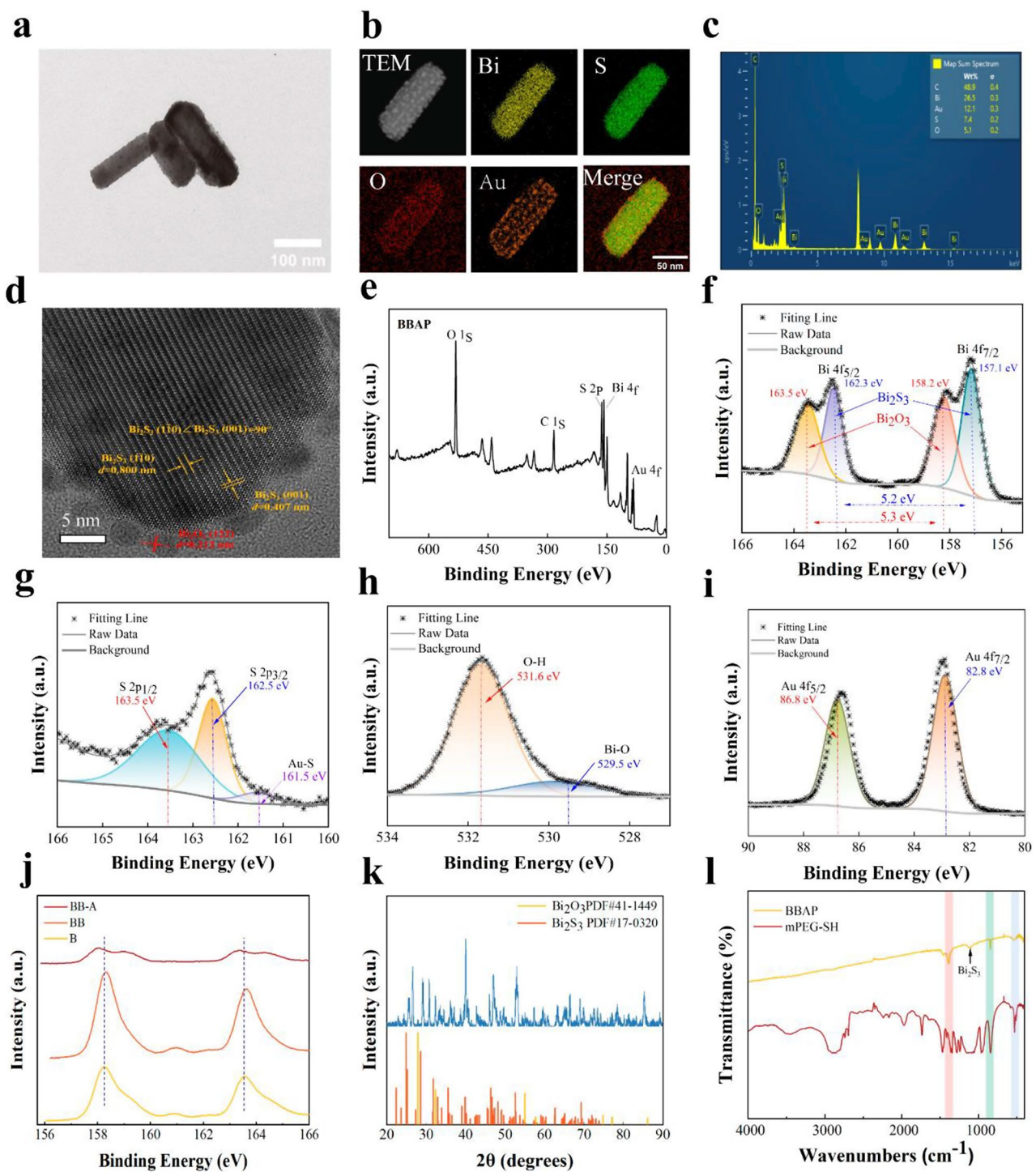
Fig. 1 Characterization. (**a**) TEM image of BB-A-P NRs. (**b**) Elemental mapping of BB-A-P NRs. (**c**) Energy-dispersed spectrum of BB-A-P NRs. (**d**) HR-TEM. (**e**) Survey XPS spectra of BB-A-P NRs. High-resolution XPS spectra of (**f**) Bi 4f, (**g**) S 2p, (**h**) O-H, Bi-O and (**i**) Au 4f in BB-A-P NRs. (**j**) Shifts of Bi 4f. (**k**) XRD pattern. (**l**) FTIR spectrum of the BB-A-P and mPEG-SH

was detected after envelopment with mPEG-SH, with the average value changing from 14.3 mV before wrapping to -19.6 mV (Figure S1). The Fourier analysis revealed that in BB-A-P, the peak at 1104 cm^{-1} is characteristic of Bi_2S_3, while the peaks near 844 cm^{-1} and 530 cm^{-1} may

be due to the superposition of Bi-O stretching vibration over C-S stretching vibration. This suggests that physical adsorption has occurred (Fig. 1l) and confirms the presence of mPEG-SH coating on the surface of BB-A-P NRs. The size of BB-A-P NRs was determined to be 113.07 nm

using dynamic light scattering (DLS) (Figure S2). In addition, the size distribution of BB-A-P NRs in various solutions was measured by DLS within 24 h (Figure S3). The particle size of BB-A-P NRs had no obvious changes in different media and remained stable during 24 h. The effective range of the enhanced permeation and retention (EPR) effect is 20–200 nm [29]. The DLS measurement results are within this range. The efficiency of photocatalysis depends on the thermodynamic and kinetic balance of the processes involved. Single-component photocatalysts face the challenge of achieving both a wide range of light absorption and a strong redox capacity because a wide range of light absorption requires narrowing the band gap of the semiconductor, while a strong redox capacity requires widening the band gap of the semiconductor [30].

Catalytic properties of the semiconductor heterostructure BB-A-P

The catalytic properties of BB-A-P NRs were evaluated following the successful synthesis of solid electron-mediated Z-scheme heterostructured semiconductor nanomaterials. BB-A-P generates O_2 and ROS by electron and hole transfer (Fig. 2a) [10, 31]. The study investigates the mechanisms of electron transfer in BB-A-P semiconductor heterostructures induced by NIR. The results show that when NIR irradiates the BB-A-P NRs, the h^+ on the VB of Bi_2S_3 and the e^- on the CB of Bi_2O_3 e^- migrate rapidly to the Au NPs, a solid-state conductor, to annihilate. This process improves the separation of e^- and h^+ of Bi_2O_3 and Bi_2S_3. The energy levels of the Z-scheme heterostructured material, composed of two different semiconductors (Bi_2O_3 and Bi_2S_3) and solid electronic dielectrics (Au NPs), are well-matched. This material effectively achieves the spatial separation of electron-hole pairs and retains strong redox active sites. As a result, the efficiency of O_2 and ROS generation under NIR light irradiation is improved (Fig. 2b) [32]. To compare the difference in CAT-like activity between BB and BB-A-P, we measured O_2 generation in deoxygenated deionized water using a dissolved oxygen meter (Fig. 2c). After NIR (1.2 W/cm^2) irradiation, the dissolved concentration of O_2 in the solution system of BB and BB-A-P exhibited strong catalase-like activity. The O_2 production reached 25.63 mg/mL at 30 min. Due to the absence of the medium, the e–h$^+$ pairs of BB underwent partial compound, weakening the catalase-like activity. As a result, the ability to produce oxygen was significantly weaker than the BB-A-P. It has been demonstrated that the e–h$^+$ separation of Z-scheme heterostructure semiconductors with solid electronic media is higher than that of conventional Z-scheme heterostructures. Additionally, during the experiment, bubbles that last longer were observed on the wall of the test tube containing BB-A-P NRs that

had been irradiated by NIR for a short period (Fig. 2c). Refractory tumors often share a common characteristic which is hypoxic tumor environment. This environment is also a significant factor in tumor metastasis [33]. BB-A-P not only has the ability to produce O_2 to alleviate the hypoxic situation within the tumor, but it also has outstanding oxidase-like (OXD-like) activity due to the large number of uncompounded e^-. This provides a greater possibility for better conversion of O_2 to $^1O_2$, achieving the purpose of generating $^1O_2$ without relying on O_2 in TEM. The catalytic mechanism of BB-A-P was investigated by characterizing ROS production using electron spin resonance spectroscopy (ESR) and chemical probes. Results were obtained through ESR spectroscopy, which utilized 2, 2, 6, 6-tetramethylpiperidine (TEMP) as a $^1O_2$ trapping agent. The characteristic ESR spectral intensity ratio of 1:1:1 was assigned to $^1O_2$ (Fig. 2d). Irradiation by NIR triggers a further separation of e^- and h^+, producing a sharp increase in the oxidation reaction of e^-, generating superoxide anion ($\cdot O_2^-$) through the production of O_2, due to its own mutation and reaction with other molecules [34]. The irradiation by NIR triggers a further separation of electrons and holes, resulting in a sharp increase in electron oxidation by generating $\cdot O_2^-$ with O_2 in H_2O. This is due to its self-dismutation and reaction with other molecules, promoting the production of $^1O_2$ [34]. However, the tendency increased significantly after the addition of H_2O_2 due to insufficient O_2 in the system. This was attributed to the fact that $^1O_2$ was mainly produced by the oxidation of $\cdot O_2^-$ by h^+. It was demonstrated that in an environment with high H_2O_2 expression, NIR irradiated BB-A-P to produce O_2. The isolated e^- further produced $\cdot O_2^-$, while NIR promoted the production of $^1O_2$. DPBF is a fluorescent indicator that is specific for $^1O_2$ and $\cdot O_2^-$. The study examined the rate of absorbance decrease of BB and BB-A-P with DPBF after NIR irradiation for different durations in an H_2O_2 environment using UV-Vis spectrophotometry (Fig. 2e). The results showed that the redox capacity of the Z-scheme heterostructure of BB-A-P was significantly enhanced compared to the normal heterostructure with the addition of the intermediary medium Au. A special probe for the $^1O_2$ measurement, the Single Online State Oxygen Sensor Green (SOSG), has been used (Fig. 2f). The peak values of the measured curves increased as the irradiation time increased. We conducted additional research on BB-A-P's ability to produce •OH in vitro, which was detected using ESR spectroscopy. 5, 5-dimethyl-1-pyrroline-N-oxide (DMPO) was chosen as the trapping agent for •OH. The characteristic ESR spectrum intensity ratio of 1:2:2:1 was assigned to •OH (Fig. 2g). The strongest characteristic peak was observed after excitation by NIR in an H_2O_2 environment. Subsequently, we used 3, 3′, 5, 5′-tetramethylbenzidine (TMB) as a colorimetric probe
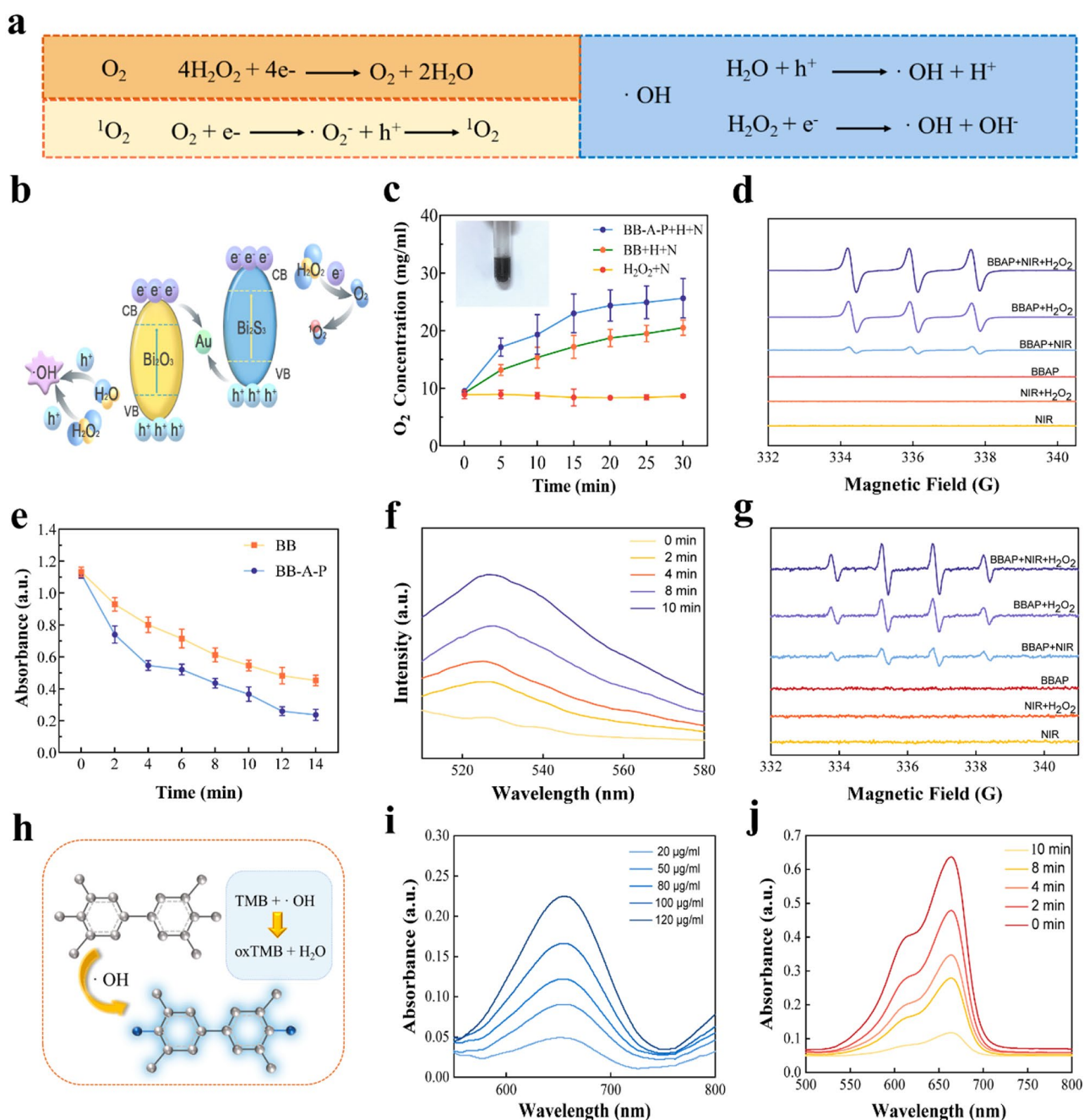
Fig. 2 Electron transfer pathways for O_2 and ROS generation by BB-A-P NRs. (**a**) Mechanisms of O_2 and ROS generation by BB-A-P NRs. (**b**) Electron-hole transfer in Z-Scheme Systems with Solid State Electron Mediators Heterostructure Semiconductor Nanomaterials under NIR. (**c**) O_2 production of BB-A-P over a time gradient ($n=3$). (**d**) TEMP-captured ESR spectra of $^1O_2$. (**e**) Absorption decay curve of DPBF at 410 nm ($n=3$). (**f**) SOSG probe to detect the $^1O_2$ generation capacity of BB-A-P NRs under NIR irradiation. (**g**) DMPO-captured ESR spectra of •OH. (**h**) Schematic representation of the TMB probe reacting with •OH to produce blue oxTMB. (**i**) •OH generation ability of BB-A-P NRs -mediated detected by the TMB probe. (**j**) •OH generation by BB-A-P NRs under NIR excitation detected by MB probes

to evaluate the production of departing •OH under NIR irradiation. The colorless TMB reacted with •OH to form blue oxidized TMB (oxTMB) (Fig. 2h). Ultraviolet-visible spectrophotometry (UV-Vis) revealed a typical absorption peak at 652 nm (Fig. 2i). The intensity of the peak increased with increasing BB-A-P concentration,

indicating a positive correlation between the concentration of BB-A-P and the yield of •OH produced by peroxidase-like (POD-like) activity. Methylene blue (MB) can be used as an anoxidative probe for ROS. This was applied to analyze the ROS release from BB-A-P after NIR irradiation. In the presence of H_2O_2 (5 mM), with

increasing NIR exposure time (1.2 W/cm^2), the characteristic absorption peak of MB at 664 nm decreased significantly (Fig. 2j). This indicates that NIR-triggered e–h$^+$ separation leads to ROS production. Our synthesized Z-scheme heterostructured semiconductors, containing solid conductor media, can mimic the functions of various enzymes by NIR excitation to produce O$_2$ and a variety of ROS. This technology has the potential to be used in a variety of applications.

BB-A-P alleviates hypoxia and the ability to produce ROS in vitro

We conducted cellular-level experiments to validate the O$_2$ and ROS-producing ability of BB-A-P and its tumor cell-killing ability. We verified the ability of BB-A-P to be taken up by cells using CLSM and flow cytometry analysis, as the cellular uptake rate of the material is crucial for its therapeutic effect. After co-culturing B16F10 cells with fluorescein isothiocyanate (FITC)-labeled BB-A-P, intense green fluorescence was observed at 6 h (Fig. 3a). The uptake capacity at 6 h was nearly 100 times higher
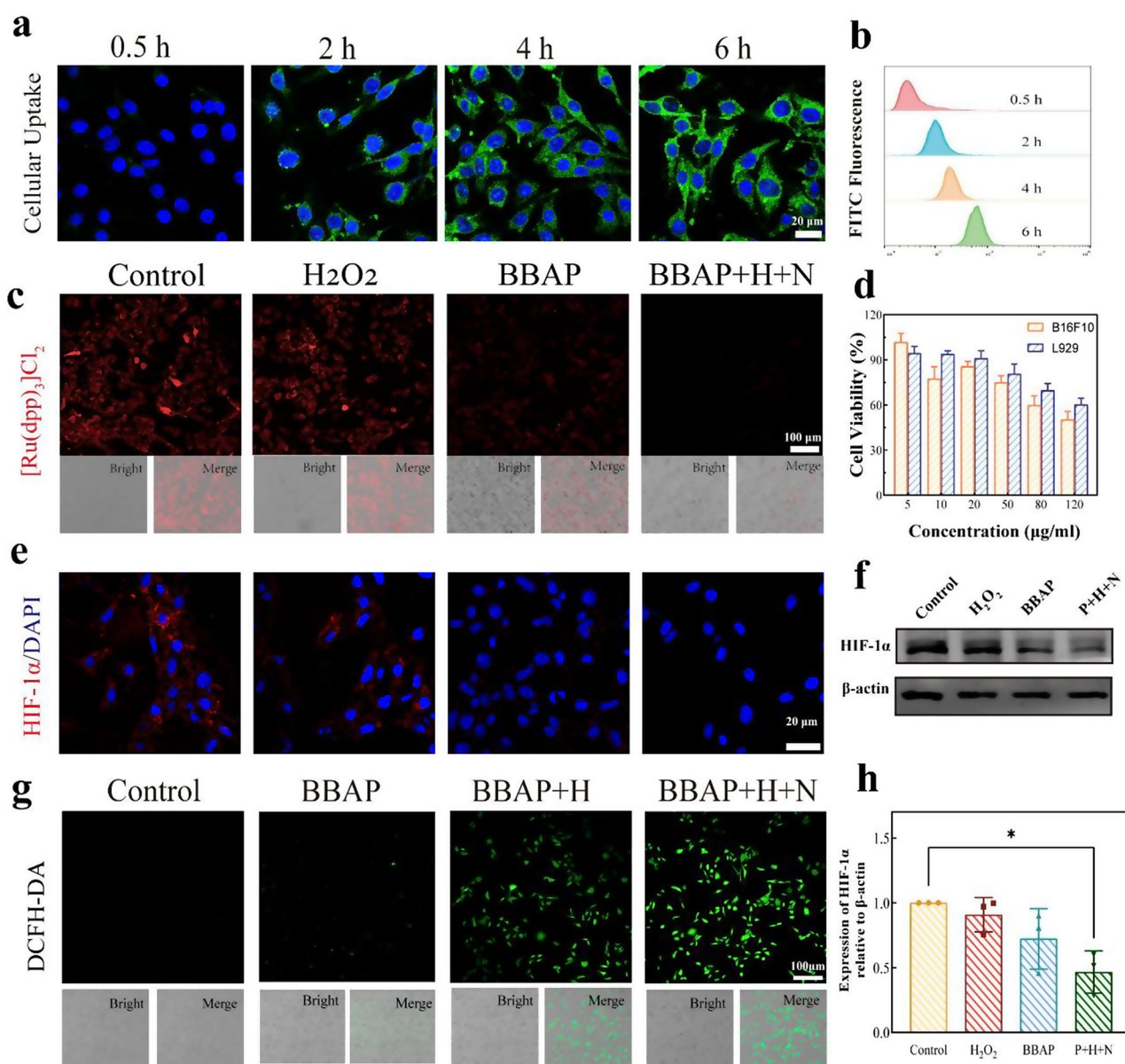

Fig. 3 In vitro antitumor effects of BB-A-P NRs. (**a**) Cellular uptake of BB-A-P NRs in B16F10 cells after different time intervals. (**b**) Cellular uptake capacity analyzed by flow cytometry using FITC fluorescence intensity. (**c**) CLSM observation of intracellular hypoxia levels in B16F10 cells utilizing the [Ru(dpp)$_3$]Cl$_2$ probe. (**d**) Cell viability of B16F10 and L929 cells treated with varied concentrations of BB-A-P NRs ($n=3$). (**e**) CLSM images showing immunofluorescence staining for HIF-1α in B16F10 cells in different subgroups. (**f**) Western blot experiment of HIF-1α in B16F10 cells in different groups. (**g**) Intracellular ROS level. (**h**) Quantitative analysis corresponding to f) ($n=3$)

than that at 0.5 h, as shown by flow cytometry analysis (Fig. 3b). A cell counting kit (CCK-8) was then used to evaluate the biosafety of BB-A-P with B16F10 melanoma cells and L929 mouse fibroblasts (Fig. 3d). At a concentration of 120 μg/mL, the average survival rate reached an average of 50.25% and 60.26% after 24 h of co-incubation with normal and melanoma cells, respectively. This suggests that BB-A-P is biocompatible and may be used for subsequent treatment. We studied the intracellular O_2 production of B16F10 cells in four groups, control group, H_2O_2 group, BB-A-P group, and BB-A-P+H_2O_2+NIR group, using tris (4, 7-diphenyl-1, 10-phenanthroline) ruthenium (II) dichloride ([Ru(dpp)$_3$] Cl$_2$) luminescence O_2 sensor and HIF-1α antibody. Since the concentration of H_2O_2 in tumors is $(50–100) \times 10^{-6}$ M, we simulated an intra-tumor environment of 100×10^{-6} M [35]. The red fluorescence of [Ru(dpp)$_3$] Cl$_2$ can be quenched by O_2, allowing for the assessment of O_2 production (Fig. 3c). There was a slight quenching of fluorescence in the presence of only BB-A-P due to its slightly weaker CAT-like activity. After being irradiated by NIR (1.2 W/cm^2), the red fluorescence was significantly reduced in the intra-tumoral environment of H_2O_2 overexpression. This suggests that the CAT-like activity of BB-A-P was stimulated by NIR irradiation and reacted with H_2O_2 in the environment ($2H_2O_2 + 4e^- \rightarrow 2H_2O + O_2 \uparrow$). Hypoxia-inducible factors (HIFs) regulates multiple signaling pathways that promote angiogenesis, metastasis, and invasiveness of tumor cells [36, 37]. A major challenge in tumor therapy is tumor invasion and metastasis [38, 39]. Alleviating the intracellular hypoxic environment and reducing the expression of HIF-1α can somewhat inhibit the proliferation and metastasis of tumor cells. To evaluate the expression level of HIF-1α in cells, we performed HIF-1α immunofluorescence staining of B16F10 cells, followed by CLSM observation (Fig. 3e). The red fluorescence of BB-A-P and BB-A-P+H_2O_2+NIR groups was significantly weaker than that of the control and H_2O_2 groups. This suggests that the subunit of HIF-1α was oxidized due to the increased O_2 content in the environment, leading to a decrease in its expression. This result was also validated in the western blotting (WB) test (Fig. 3f). HIF-1α expression was weakest in the BB-A-P+H_2O_2+NIR group, which was also confirmed by the WB quantification results. There was a statistical difference between the control group and the P+H+N group (Fig. 3h). Thus, it can be inferred that the combination of BB-A-P and NIR can enhance the oxygen content in tumor cells and the overall hypoxic condition of the tumor [40, 41]. We also investigated the capacity of BB-A-P to generate ROS within the cells. It is known that 2′, 7′-dichlorodihydrofluorescein diacetate (DCFH-DA) is easily broken down by ROS, resulting in bright green fluorescence. The fluorescence intensity is directly proportional to the amount of ROS generated within the cell. In the BB-A-P group, only a small amount of ROS was produced due to its reaction with intracellular H_2O and a small amount of H_2O_2 (Fig. 3g). Subsequently, the green fluorescence intensity significantly increased by simulating the concentration of H_2O_2 within the tumor. After adding NIR irradiation, the separation of e$^-$ and h$^+$ was sufficiently stimulated, increased ROS generation. The produced e$^-$ and h$^+$ reacted with H_2O_2 and H_2O in sufficient redox reactions to produce ROS, resulting in the strongest green fluorescence. Meanwhile, we treated the cells under identical conditions and confirmed this through flow cytometry analysis (Figure S4).

In vitro BB-A-P damage to mitochondria and antitumor capacity

After evaluating the biosafety of BB-A-P and its ability to generate oxygen and ROS, we subsequently verified its ability to kill tumor cells intracellularly and cause alterations in mitochondrial membrane potential. Excessive oxidative stress resulting from the overproduction of ROS can lead to impairments in mitochondrial function and cell development [42, 43]. Numerous studies have demonstrated the close association between mitochondria and apoptosis. Disruption of the mitochondrial transmembrane potential (ΔΨm) is one of the earliest events in the apoptotic cascade response, occurring before the appearance of apoptotic features such as chromatin condensation and DNA breaks. Once the mitochondrial transmembrane potential collapses, apoptosis is irreversible. First, we verified the alteration of mitochondrial membrane potential (MMP) by BB-A-P. This compound exhibits a high ΔΨm in normal and undamaged nucleated cells. The disruption of ΔΨm is characteristic of early apoptosis [44]. JC-1 exists in two states: monomer and multimer. At low concentrations, it exists as a monomer and at high concentrations, it exists as a multimer. Both states have different emission spectra, but they can be detected as green fluorescence in the FL-1 channel of the flow cytometer. The multimers emit red fluorescence, which can be detected by the red (FL-2) channel of the flow cytometer. During apoptosis, the mitochondrial transmembrane potential is depolarized, and JC-1 is released from the mitochondria, causing the intensity of the red light to weaken. JC-1 exists as a monomer in the cytoplasm and emits green fluorescence. The control and H_2O_2+NIR groups exhibited intense red and green fluorescence (Fig. 4a). The addition of BB-A-P resulted in a lesser attenuation of the red fluorescence, indicating a low production of ROS that did not reach the threshold concentration for damage. In the subsequent experimental group, we added H_2O_2 and NIR. We found that the red fluorescence of the experimental group with both conditions significantly weakened, and a clear green
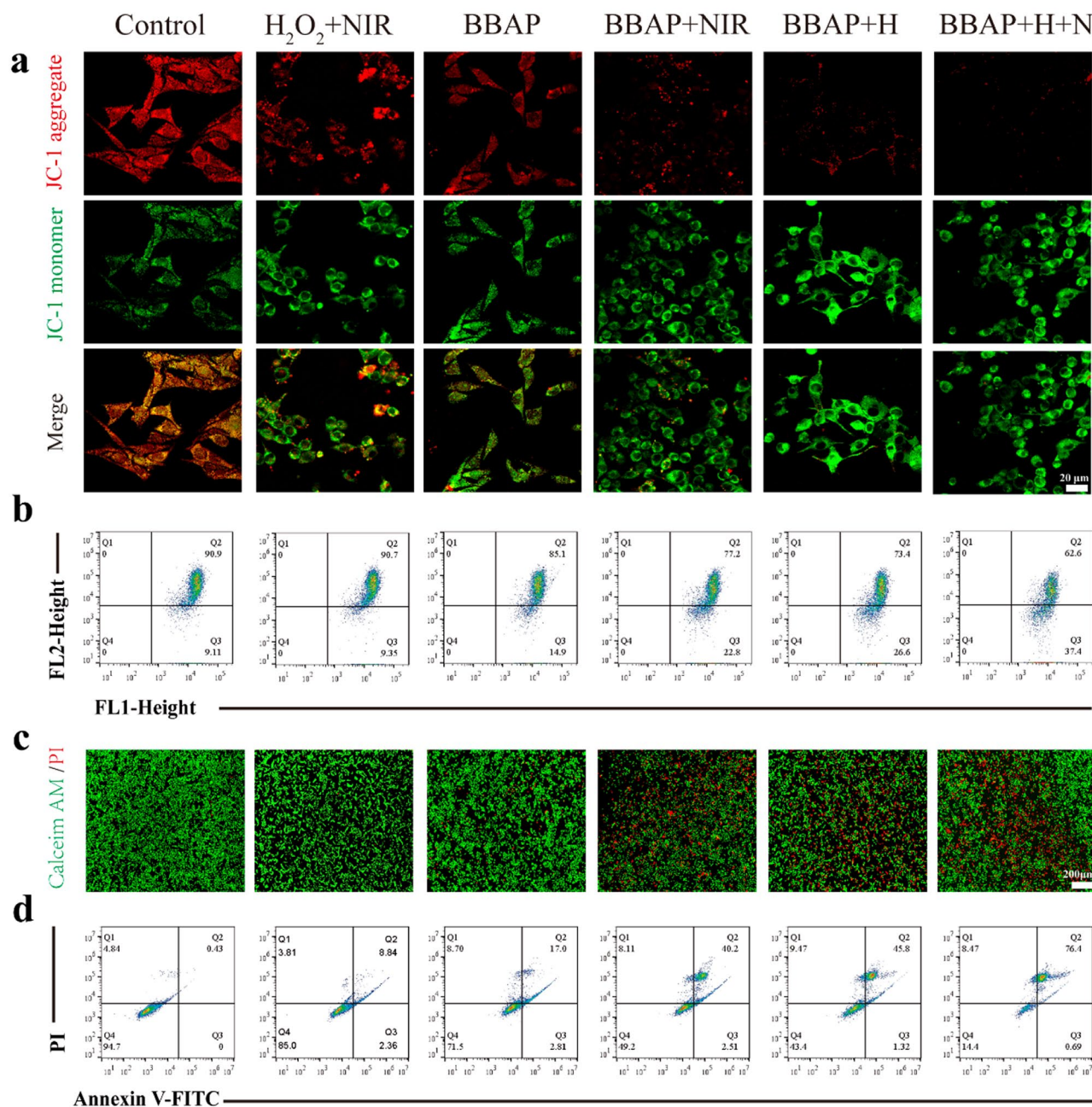
Fig. 4 (**a**) JC-1 detects mitochondrial membrane potential in B16F10 cells. (**b**) JC-1 flow cytometry analysis of mitochondrial membrane potential. (**c**) Intracellular live/dead staining of B16F10 cells after different treatments. (**d**) Apoptosis of B16F10 cells after different treatments analyzed by Annexin V-FITC/PI flow cytometry

fluorescence was visible. This result proves that NIR promoted the ability of BB-A-P to produce ROS and simultaneously decomposed H_2O and H_2O_2 in the environment, generating a sufficient amount of ROS to lead to the depolarization of MMP. The results of the flow cytometry analysis showed Q2 and Q3 percentages ranging from 90.9 to 62.6% and 9.11–37.4%, respectively (Fig. 4b), confirming the depolarization of MMP. To verify the killing ability of BB-A-P on tumor cells, we stained live and dead

cells using calcein AM and propidium iodide (PI), respectively. Live cells were stained green, while dead cells were stained red (Fig. 4c). In the control group and H_2O_2+NIR group, almost no red fluorescence was observed, while a small amount of red fluorescence was seen in the BB-A-P group, indicating that only a few cells died. Upon adding H_2O_2 or NIR, the proportion of red fluorescence increased significantly. In the BB-A-P+H_2O_2+NIR group, a large area of red fluorescence was observed,

demonstrating that BB-A-P has a more vital ability to kill tumors. It is important to note that these results are objective and based solely on the observed data. We used flow cytometry analysis (Annexin V-FITC/ PI-based apoptosis analysis) to verify that the proportion of early and late apoptosis of B16F10 in the BB-A-P+H_2O_2+NIR group was 77.09%, which was consistent with the trend of live/dead cell experiment (Fig. 4d).

Immunogenic pyroptosis triggered by BB-A-P

The study aimed to investigate whether cellular pyroptosis is responsible for tumor cell death induced by BB-A-P.

We observe the cell morphology under the microscope. After co-incubation with BB-A-P, we divided the cells into three groups, NIR, H_2O_2, and NIR+H_2O_2 (Fig. 5a). Only the group treated with NIR showed slight deformation and swelling of the cells. The addition of H_2O_2 resulted in the appearance of a small number of cell vacuoles, which is a typical manifestation of cellular pyroptosis. The NIR+H_2O_2 group showed an increased number of cells with cellular vacuoles and more pyroptosis cells appeared compared with the previous two groups, indicating that BB-A-P-induced pyroptosis while inducing apoptosis of tumor cells, which was a significant finding
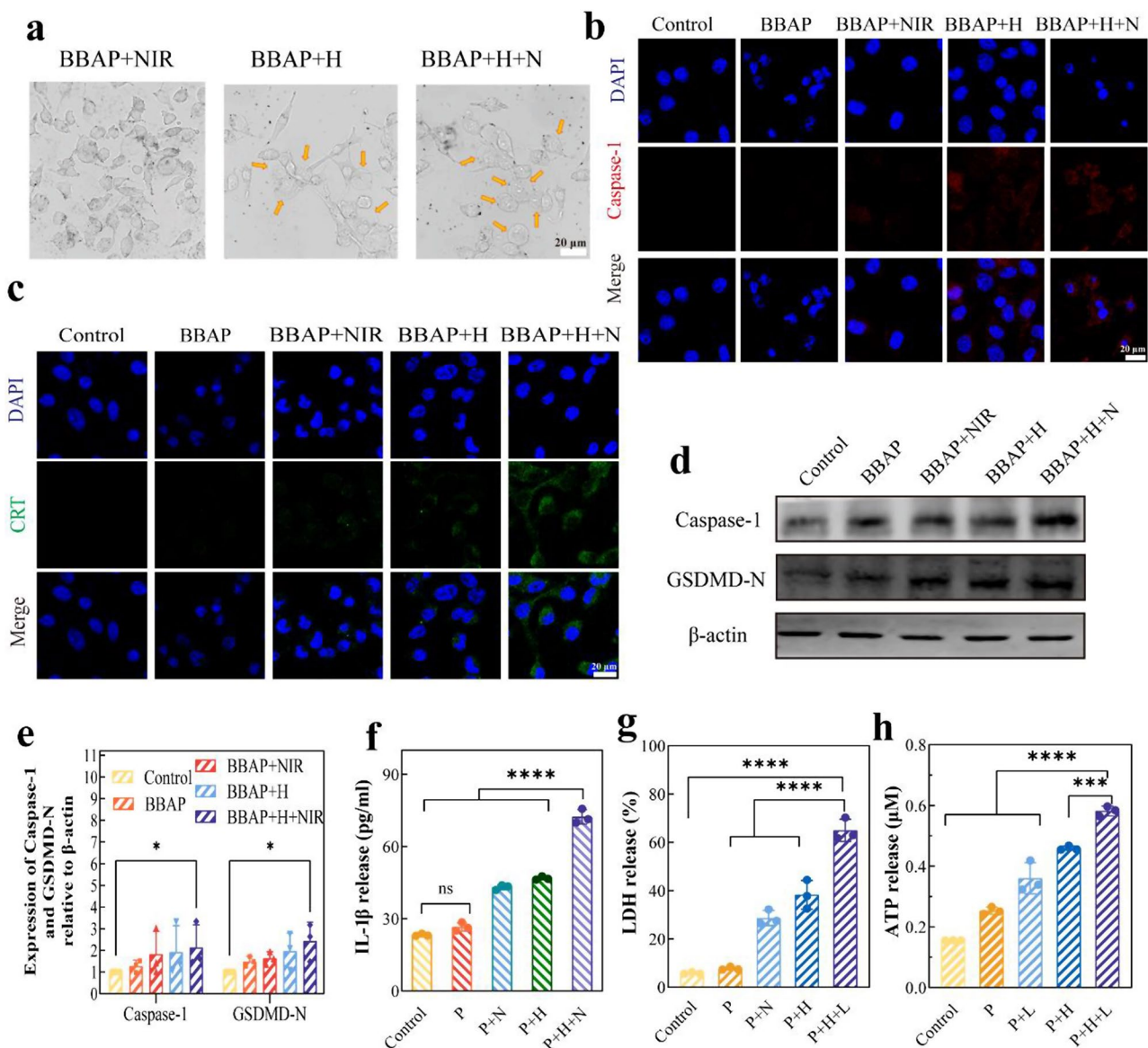

Fig. 5 (**a**) Morphological images of B16F10 cells from different treatments. Cells were swollen with large bubbles (yellow arrows). (**b**) Immunofluorescence of Caspase-1 under different treatments. (**c**) Immunofluorescence of CRT under different treatments. (**d**) Western blots of Caspase-1 and GSDMD-N expressions. (**e**) Quantitative analysis corresponding to d) (*n*=3). (**f**) IL-1β expression after different treatments (*n*=3). (**g**) LDH expression after different treatments (*n*=3). (h) ATP release after different treatments (*n*=3)

Ren *et al. Journal of Nanobiotechnology*   (2024) 22:526

Page 14 of 18

in our study. Under co-treatment with BB-A-P, NIR and H_2O_2, tumor cells undergo cellular pyroptosis. This led to the disruption of the integrity of the B16F10 cell membrane, triggering the release of subsequent cellular contents, including pro-inflammatory factors and related antigens, into the tumor microenvironment. The cleavage of GSDMD by Caspase-1 is considered a critical process that causes pyroptosis. B16F10 cells were observed under CLSM after various treatments. The intensity of red fluorescence was used to represent the level of Caspase-1 expression (Fig. 5b). The strongest red fluorescence was observed in the presence of both H_2O_2 and NIR. This result suggests that BB-A-P induces pyroptosis through the typical Caspase-1/GSDMD pathway. Meanwhile, the expression of GSDMD-N followed the same trend as Caspase-1. This was also confirmed by WB experiments (Fig. 5d) and WB quantification experiments (Fig. 5e). As evidenced by the experimental results, there is statistical disparity between the BB-A-P combined NIR group and the control group. ICD is a crucial aspect of programmed cell death. When tumor cells undergo ICD, they release DAMPs, like CRT and ATP. These molecules serve as typical markers of immunogenic death and play essential roles in antigen presentation and in synergizing the immune response [45, 46]. Fortunately, significant changes in both CRT and ATP were detected during the induction of cellular pyroptosis. Under CLSM, both the BB-A-P+NIR and BB-A-P groups exhibited weak green fluorescence, while the fluorescence of the other groups was significantly weaker than that of the BB-A-P+H_2O_2+NIR group (Fig. 5c). The results of the ATP release experiments show a significant difference between the experimental group and the control group. Additionally, the BB-A-P+H_2O_2 group has a significant difference with BB-A-P+H_2O_2+NIR (Fig. 5h), which verifies the ICD effect. Meanwhile, cellular pyroptosis often results in the release of a large number of inflammatory molecules, such as interleukin-1β (IL-1β) and lactate dehydrogenase (LDH) (Fig. 5f-g). The results showed that BB-A-P stimulated the release of IL-1β, and BB-A-P+H_2O_2+NIR was significantly different from other groups. However, there was no significant difference between the control and BB-A-P groups. (Fig. 5f). These findings suggest that BB-A-P combined with NIR creates a favorable condition for inducing pyroptosis. In the LDH release experiment, the results showed a statistically significant difference between P+H+N and the control group (Fig. 5g). Additionally, significant differences were observed between the BB-A-P, BB-A-P+NIR, BB-A-P+H_2O_2, and BB-A-P+H_2O_2+NIR group, indicating that BB-A-P may have a more significant impact on inducing tumor cellular pyroptosis in the tumor microenvironment under near-infrared light irradiation. It is worth noting that cellular pyroptosis, a programmed death pathway, plays a crucial

role in activating tumor immunogenic death. By releasing cellular contents that are pro-inflammatory, it offers the possibility of activating immunotherapy for tumors [47, 48].

In vivo antitumor studies

The antitumor effects of BB-A-P were tested in the B16F10 tumor-bearing model. To define the timing of NIR light treatment more clearly, we investigated the biodistribution and accumulation of BB-A-P in mice. Bi content in major organs and tumor tissues at different times (1, 3, 6, 24, 48 h) after intravenous injection of BB-A-P was detected using inductively coupled plasma emission spectrometry (ICP-OES) (Fig. 6b). Due to the typical EPR effect, BB-A-P can accumulate in tumor tissues. The start of NIR irradiation after intravenous BB-A-P can be determined based on accumulation. Secondly, we co-cultured mouse erythrocytes with different concentrations of BB-A-P (1.56, 3.13, 6.25, 12.50, 25, 50, 100 µg/mL) in PBS solution and deionized water. The absorbance at 541 nm was measured by UV-visible spectrophotometer to obtain the corresponding hemolysis rate. Deionized water was used as a positive control (hemolysis rate=100%) (Figure S5). Even at a concentration of 100 µg/mL, the hemolysis rate of BB-A-P remained below 20%, indicating its effectiveness for intravenous treatment. Afterwards, the B16F10 tumor-bearing mice were randomly assigned to one of four groups (n=5): control, NIR, BB-A-P, and BB-A-P+NIR. Treatment was administered to each group on days 1 and 3. The intravenous dose was 5 mg/kg, followed by NIR light irradiation (808 nm, 1.2 W /cm^2, 10 min) 24 h after injection (Fig. 6a). The body weight and tumor volume of each mouse were measured and recorded every 2 days throughout the treatment (Fig. 6c, e). The study results indicate that the tumor volume of BB-A-P alone was smaller than that of the control group. In contrast, the tumor growth of mice in the BB-A-P+NIR group was significantly inhibited, more so than in the other groups, and did not cause weight loss. Our synthesized BB-A-P nano-enzymes induced dual programmed death, resulting in a strong synergistic effect. The average weight of the dissected tumors (Fig. 6d) and visualized photographs (Figure S6) demonstrate this superior synergistic therapeutic effect. The experimental results show that the BB - A - P+NIR group and other groups have significant statistical difference (Fig. 6d). In addition, there has been a significant improvement in the survival rate of the mice after treatment (Fig. 6f). Blood was taken from various groups of mice to determine their hematological index (Figure S7) and liver and kidney functions (Figure S8). The study found no statistically significant difference between the experimental group and the control group. Hematoxylin-eosin (H&E) staining was used to examine
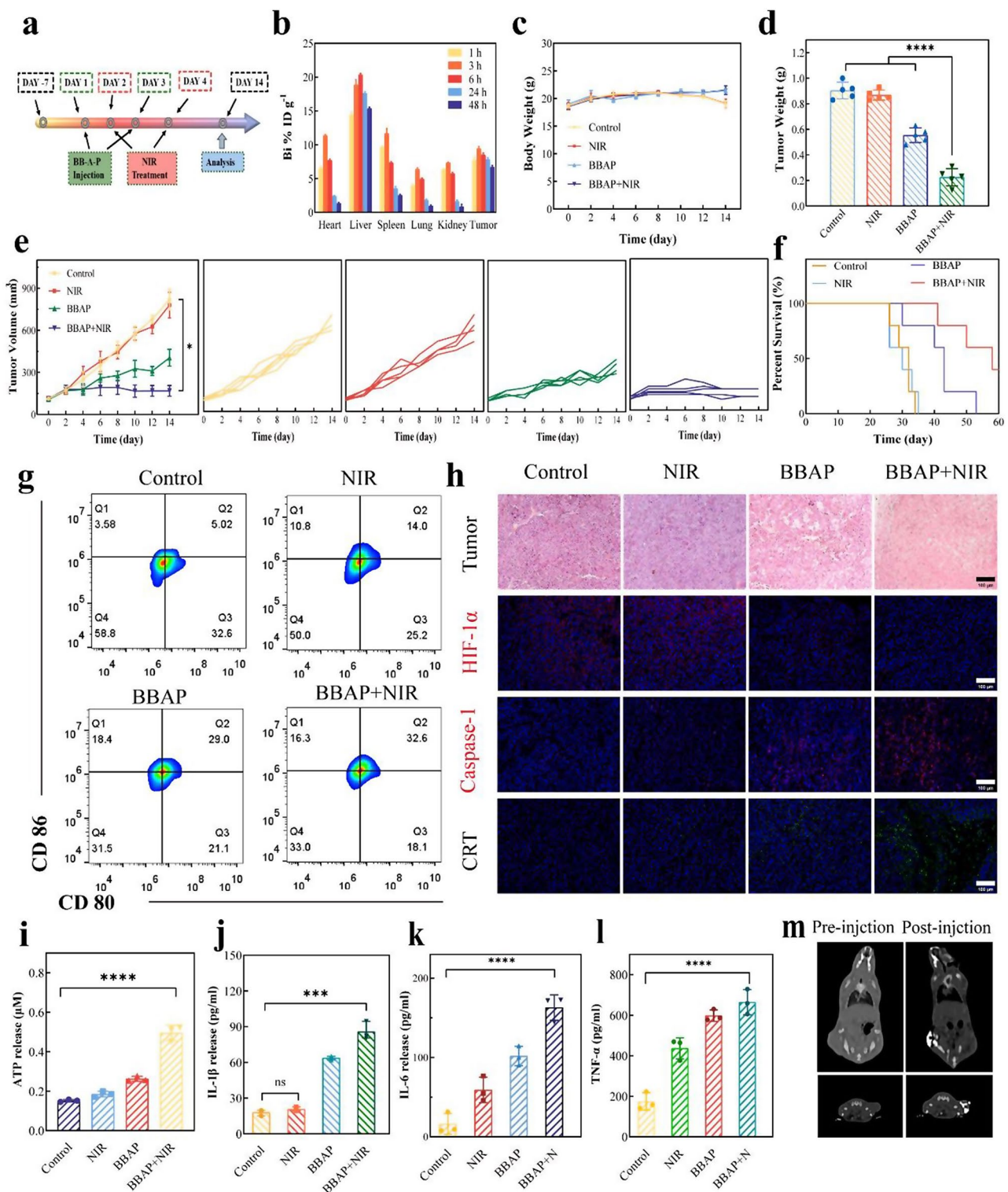
Fig. 6 In vivo anti-tumor effects of BB-A-P NRs (n = 5). (**a**) Schematic representation of treatment time in tumor-bearing mice. (**b**) Biodistribution of Bi concentrations in mice measured at different time (n = 3). (**c**) Body weight over time (n = 5). (**d**) Tumors' weights (n = 5). (**e**) Tumor volume after different treatments (n = 5). (**f**) Survival curves of mice receiving treatments (n = 5). (**g**) Flow cytometer detects dendritic cell maturation. (**h**) Staining of H&E, HIF-1α, Caspase-1 and CRT in tumor tissues of different treatment groups. (**i**) ATP release after different treatments (n = 3). (**j**) IL-1β expression after different treatments (n = 3). (**k**) IL-6 release after treatments(n = 3). (**l**) TNF-α expression after treatments(n = 3). (**m**) CT imaging

the heart, liver, spleen, lungs, and kidneys of the mice, and no significant abnormalities were observed (Figure S9). This shows that BB-A-P treatment did not significantly affect the vital organs. Tumor killing ability was confirmed through H&E staining, immunofluorescence staining of dissected tumor tissues from various groups (Fig. 6h). The therapeutic effects of different treatments on the tumors were evaluated using the H&E staining technique. Compared to the other three groups, the BB-A-P+NIR group exhibited the most severe tumor necrosis and damage, which inhibited tumor growth. The BB-A-P+NIR group showed the most significant green fluorescence expression under an inverted fluorescence microscope by Tunel kit staining, indicating a significantly increased proportion of apoptotic cells in this group compared to the other three groups (Figure S10). Immunohistochemistry revealed that the expression of the value-added marker Ki-67 was similarly down-regulated in the BBAP+NIR group, indicating a decrease in the proliferative capacity of tumor cells (Figure S10). This demonstrates that the treatment of BB-A-P+NIR inhibited the growth of tumor cells. To evaluate the ability of NIR-excited BB-A-P to reverse tumor hypoxia, we assessed the expression of HIF-1α in tumor tissues in different groups using HIF-1α immunofluorescence staining. The BB-A-P+NIR group exhibited the weakest fluorescence intensity. The results suggest that under NIR stimulation, BB-A-P can catalyze the cleavage of water and H_2O_2 through the action of the special Z-scheme heterostructure CAT-like. This increases the supply of O_2 and improves hypoxia within the tumor, thereby reducing the accumulation of HIF-1α (Fig. 6h). Caspase-1 is an important factor in inducing cellular pyroptosis. The results of the immunofluorescence assay showed that Caspase-1 expression was strongest (red fluorescence) in the BB-A-P+NIR group compared to the other three groups, indicating cellular pyroptosis occurred during BB-A-P treatment (Fig. 6h). Additionally, important markers of DAMPs, CRT and ATP showed statistically significant differences from the control group in the treated group. The tumor tissues of the BB-A-P+NIR treatment group exhibited the most intense green fluorescence (CRT) (Fig. 6h). Additionally, we observed a release of ATP in the serum of mice (Fig. 6i). The BB-A-P+NIR group showed approximately four times higher levels of ATP release compared to the control group, with a statistically significant difference. The elevation of these DAMPs can promote antigen presentation and synergize immunotherapy. During the process of pyroptosis in the tumor, there was a significant increase in corresponding inflammatory factors, such as IL-1β. This cytokine showed the strongest expression in all four groups in the BB-A-P+NIR group, moreover, there was a significant statistical difference between BB-A-P+NIR group and control group. While the control group and NIR group had no obvious difference. (Fig. 6j). Subsequently, we used flow cytometry to assess the level of tumor immune cell infiltration in the lymph nodes of mice from different treatment groups. Enhancing the maturation of DCs is crucial for promoting antigen presentation and T-cell activation. According to flow cytometry analysis, BB-A-P was found to promote DCs maturation approximately 6.5 times more than the control group (Fig. 6g). These results suggest that the combination of BB-A-P and NIR treatment can stimulate DCs maturation, induce tumor cell pyroptosis, and further enhance T-cell activation. Consequently, we conducted a further evaluation of the alterations in the CD4$^+$ T cells and CD8$^+$ T cells content within the spleens of mice in different groups (Figure S11). Consequently, the combination of BB-A-P NRs and NIR treatment was found to effectively induce the activation of helper T cells and cytotoxic T lymphocytes. Serum samples was collected from various treatment groups to evaluate the levels of two cytokines, IL-6 and TNF-α, using ELISA (Fig. 6k, l). The results of the experiment demonstrate a statistically significant discrepancy between the BB-A-P combined NIR group and the control group. The experimental group exhibited significantly stronger expression than the other three groups, indicating that the combination of BB-A-P and NIR treatment enhanced T-cell infiltration and capacity. This was validated in animal experiments on the tumor's ICD effect. Melanoma is a particularly aggressive form of tumor, and thus, there is a pressing need for more effective long-term treatment methods to inhibit tumor metastasis and recurrence. In this study, we employed a previously described modeling and treatment protocol and sacrificed mice after three days. We then harvested their spleens and evaluated CD62L/CD44 expression (Figure S12). The expression of CD62L and CD44 was significantly increased compared with the control group, indicating that BB-A-P combined with NIR treatment activated central memory T cells to achieve long-term antitumor immunity [49]. Due to the fact that the location of the tumor may not be fully visualized and the internal structure of the tumor may not be fully observed, imaging can be used to better guide therapeutic targeting during the treatment process, making tumors more complete to treat. BB-A-P nanoparticles have potential for CT imaging due to bismuth's considerable sensitivity and low cost. The construction of high-performance CT contrast agents (CAs) using BB-A-P nanoparticles is promising. Tumor signal enhancement was still observed in CT imaging 2 h after intra-tumoral injection of BB-A-P (Fig. 6m). The findings suggest that BB-A-P can be used as a safe and effective chemoresponsive nanorods to enhance synergistic dual programmed death and ICD.

Conclusions

In conclusion, this study proposes BB-A-P as a potential apoptotic and pyroptosis inducer for cancer immunotherapy. BB-A-P is a novel Z-scheme heterostructure that, upon excitation by NIR, alleviates intracellular hypoxia and ROS surges, activating the Caspase-1/GSDMD-dependent pathway, leading to pyroptosis accompanied by cell swelling and necrosis, which further promotes the release of a variety of inflammatory molecules and DCs maturation inducing ICD and inhibiting tumor cell proliferation. Necrosis promotes the release of numerous inflammatory molecules, induces ICD, and inhibits tumor cell proliferation, achieving immunotherapy. Additionally, it has CT imaging capabilities to visualize anti-tumor immune activation and tumor growth inhibition. The research will expand the biomedical applications of Bi-based nanoparticles as well as our understanding of ICD that nanomaterials induced.

Appendix A. supplementary data

The Supplementary data contain: Chemicals and Reagents, the synthesis of Bi_2S_3-Bi_2O_3 nanorods (BB NRs) composite, Zeta potentials of B, BB, BBA, BBAP ($n=3$), dynamic light scattering distribution (DLS) of BBAP, flow cytometry analysis of ROS, hemolysis rate of BB-A-P NRs at different concentrations after co-incubation with mouse erythrocytes, hormonal mice from different groups, hematological index and biochemistry of different groups of mice after 7 days BB-A-P intravenous injection, H&E-stained sections of major organs of different groups of mice, tunel and Ki-67 staining of tumor sections from different groupings of mice, and flow cytometry analysis of $CD4^+$/ $CD8^+$, CD44/ CD62L T cells in spleens from mice in various groups.

Supplementary Information

The online version contains supplementary material available at https://doi.org/10.1186/s12951-024-02770-4.

> Supplementary Material 1

Author contributions
Yiping Ren and Yun Wang designed and performed most of the experiments. Cheng Chen and Xiang Yan were involved in device fabrication and material characterization. Minghao Chao, Yuting Li, Yuqi Huang, Dehong Yu, and Xiaoyang Hou provided suggestions for the project. Yiping Ren and Yun Wang wrote and revised the manuscript. Guan Jiang, Ming Guan and Fenglei Gao supervision. All authors have given approval to the final version of the manuscript. The manuscript was written through the contributions of all authors. All authors have given approval to the final version of the manuscript.

Data availability
No datasets were generated or analysed during the current study.

Declarations

Ethics approval and consent to participate
All animal experiments were approved by the Animal Protection and Ethics Committee of Xuzhou Medical University. The ethical code of animal study is 202306T020.

Competing interests
The authors declare no competing interests.

Author details
[1]Department of Laboratory Medicine, Shanghai Medical College, Huashan Hospital, Fudan University, Shanghai 200040, China
[2]Jiangsu Key Laboratory of New Drug Research and Clinical Pharmacy, Xuzhou Medical University, Xuzhou 221004, Jiangsu, People's Republic of China
[3]Department of Dermatology, Affiliated Hospital of Xuzhou Medical University, Xuzhou 221002, Jiangsu, People's Republic of China
[4]Department of Dermatology, The Second People's Hospital of Huai'an, The Affiliated Huai'an Hospital of Xuzhou Medical University, Huai'an 223002, China

References
1. Xue S, Ruan G, Li J, Madry H, Zhang C, Ding C. Bio-responsive and multi-modality imaging nanomedicine for osteoarthritis theranostics. Biomater Sci. 2023;11(15):5095–107.
2. Bechet D, Couleaud P, Frochot C, Viriot M-L, Guillemin F. Barberi-Heyob, Nanoparticles as vehicles for delivery of photodynamic therapy agents. Trends Biotechnol. 2008;26(11):612–21.
3. Cao L, Sahu S, Anilkumar P, Bunker CE, Xu J, Fernando KAS, Wang P, Guliants EA, Tackett KN, Sun Y-P. Carbon nanoparticles as visible-light photocatalysts for efficient CO_2 conversion and beyond. J Am Chem Soc. 2011;133(13):4754–7.
4. Qiao R, Mao M, Hu E, Zhong Y, Ning J, Hu Y. Facile formation of mesoporous $BiVO_4$/Ag/AgCl heterostructured microspheres with enhanced visible-light photoactivity. Inorg Chem. 2015;54(18):9033–9.
5. Pan C, Ou M, Cheng Q, Zhou Y, Yu Y, Li Z, Zhang F, Xia D, Mei L, Ji X. Z-Scheme heterojunction functionalized pyrite nanosheets for modulating tumor microenvironment and strengthening photo/chemodynamic therapeutic effects. Adv Funct Mater 30(3) (2019).
6. Xiao Z, Xu C, Jiang X, Zhang W, Peng Y, Zou R, Huang X, Liu Q, Qin Z, Hu J. Hydrophilic bismuth sulfur nanoflower superstructures with an improved photothermal efficiency for ablation of cancer cells. Nano Res. 2016;9(7):1934–47.
7. Briand GG, Burford N. Bismuth compounds and preparations with biological or medicinal relevance. Chem Rev. 1999;99(9):2601–58.
8. Andrews PC, Deacon GB, Forsyth CM, Junk PC, Kumar I, Maguire M. Towards a structural understanding of the anti-ulcer and anti-gastritis drug bismuth subsalicylate. Angew Chem. 2006;45(34):5638–42.
9. Mjos KD, Orvig C. Metallodrugs in medicinal inorganic chemistry. Chem Rev. 2014;114(8):4540–63.
10. Wang X, Zhang C, Du J, Dong X, Jian S, Yan L, Gu Z, Zhao Y. Enhanced generation of non-oxygen dependent free radicals by schottky-type heterostructures of au-bi2s3 nanoparticles via x-ray-induced catalytic reaction for radiosensitization. ACS Nano. 2019;13(5):5947–58.
11. Kashmery HA, El-Hout SI. Bi_2S_3/Bi_2O_3 nanocomposites as effective photocatalysts for photocatalytic degradation of tetracycline under visible-light exposure. Opt Mater 135 (2023).
12. Cheng Y, Chang Y, Feng Y, Jian H, Tang Z, Zhang H. Deep-level defect enhanced photothermal performance of bismuth sulfide-gold

heterojunction nanorods for photothermal therapy of cancer guided by computed tomography imaging. Angew Chem. 2018;57(1):246–51.

13. Ouyang R, Cao P, Jia P, Wang H, Zong T, Dai C, Yuan J, Li Y, Sun D, Guo N, Miao Y, Zhou S. Bistratal Au@Bi$_2$S$_3$ nanobones for excellent NIR-triggered/multimodal imaging-guided synergistic therapy for liver cancer. Bioact Mater. 2021;6(2):386–403.

14. Cheng Y, Chang Y, Feng Y, Jian H, Wu X, Zheng R, Xu K, Zhang H. Bismuth sulfide nanorods with retractable zinc protoporphyrin molecules for suppressing innate antioxidant defense system and strengthening phototherapeutic effects. Adv Mater. 2019;31(10):e1806808.

15. Cheng Z, Li M, Dey R, Chen Y. Nanomaterials for cancer therapy: current progress and perspectives. J Hematol Oncol. 2021;14(1):85.

16. Evavold CL, Hafner-Bratkovič I, Devant P, D'Andrea JM, Ngwa EM, Boršić E, Doench JG, LaFleur MW, Sharpe AH, Thiagarajah JR, Kagan JC. Control of gasdermin D oligomerization and pyroptosis by the Ragulator-Rag-mTORC1 pathway. Cell 184(17) (2021).

17. Sahin U, Türeci Ö. Personalized vaccines for cancer immunotherapy. Science. 2018;359(6382):1355–60.

18. Martins F, Sofiya L, Sykiotis GP, Lamine F, Maillard M, Fraga M, Shabafrouz K, Ribi C, Cairoli A, Guex-Crosier Y, Kuntzer T, Michielin O, Peters S, Coukos G, Spertini F, Thompson JA, Obeid M. Adverse effects of immune-checkpoint inhibitors: epidemiology, management and surveillance. Nat Rev Clin Oncol. 2019;16(9):563–80.

19. Shi J, Zhao Y, Wang K, Shi X, Wang Y, Huang H, Zhuang Y, Cai T, Wang F, Shao F. Cleavage of GSDMD by inflammatory caspases determines pyroptotic cell death. Nature. 2015;526(7575):660–5.

20. Kayagaki N, Stowe IB, Lee BL, O'Rourke K, Anderson K, Warming S, Cuellar T, Haley B, Roose-Girma M, Phung QT, Liu PS, Lill JR, Li H, Wu J, Kummerfeld S, Zhang J, Lee WP, Snipas SJ, Salvesen GS, Morris LX, Fitzgerald L, Zhang Y, Bertram EM, Goodnow CC, Dixit VM. Caspase-11 cleaves gasdermin D for non-canonical inflammasome signalling. Nature. 2015;526(7575):666–71.

21. Man SM, Karki R, Kanneganti T-D. Molecular mechanisms and functions of pyroptosis, inflammatory caspases and inflammasomes in infectious diseases. Immunol Rev. 2017;277(1):61–75.

22. Tsuchiya K. Switching from apoptosis to pyroptosis: Gasdermin-elicited inflammation and antitumor immunity. Int J Mol Sci 22(1) (2021).

23. Jorgensen I, Miao EA. Pyroptotic cell death defends against intracellular pathogens. Immunol Rev. 2015;265(1):130–42.

24. Luo S, Qin F, Ming Ya, Zhao H, Liu Y, Chen R. Fabrication uniform hollow Bi$_2$S$_3$ nanospheres via Kirkendall effect for photocatalytic reduction of cr(VI) in electroplating industry wastewater. J Hazard Mater. 2017;340:253–62.

25. Drmosh QA, Hezam A, Hendi AHY, Qamar M, Yamani ZH, Byrappa K. Ternary Bi$_2$S$_3$/MoS$_2$/TiO$_2$ with double Z-scheme configuration as high performance photocatalyst. Appl Surf Sci. 2020;499:10.

26. Mahony DE, Woods A, Eelman MD, Burford N, Veldhuyzen SJO, van Zanten. Interaction of Bismuth subsalicylate with fruit juices, ascorbic acid, and thiol-containing substrates to produce soluble bismuth products active against Clostridium difficile. Antimicrob Agents Chemother. 2005;49(1):431–3.

27. Lyu ZJ, Wang F, Liu P, Zhang K, Sun Q, Bai XY, Li AX, Song XH. One-pot preparation of lutein block methoxy polyethylene glycol copolymer-coated lutein nanoemulsion. Colloid Polym Sci. 2021;299(6):1055–62.

28. Chen L, He J, Yuan Q, Liu Y, Au CT, Yin SF. Environmentally benign synthesis of branched Bi$_2$O$_3$-Bi$_2$S$_3$ photocatalysts by an etching and re-growth method. J Mater Chem A. 2015;3(3):1096–102.

29. Dai YL, Xu C, Sun XL, Chen XY. Nanoparticle design strategies for enhanced anticancer therapy by exploiting the tumour microenvironment. Chem Soc Rev. 2017;46(12):3830–52.

30. Li HJ, Tu WG, Zhou Y, Zou ZG. Z-scheme photocatalytic systems for promoting photocatalytic performance: recent progress and future challenges. Adv Sci. 2016;3(11):12.

31. Yang L, Tian B, Xie Y, Dong S, Yang M, Gai S, Lin J. Oxygen-vacancy-rich piezoelectric BiO$_{(2-x)}$ nanosheets for augmented piezocatalytic, Sonothermal and Enzymatic therapies. Adv Mater (2023) e2300648.

32. Kang Y, Li Z, Yang Y, Su Z, Ji X, Zhang S. Antimonene nanosheets-based z-scheme heterostructure with enhanced reactive oxygen species generation and photothermal conversion efficiency for photonic therapy of cancer. Adv Healthc Mater. 2021;10(3):e2001835.

33. Gilkes DM, Semenza GL, Wirtz D. Hypoxia and the extracellular matrix: drivers of tumour metastasis. Nat Rev Cancer. 2014;14(6):430–9.

34. Dickinson BC, Chang CJ. Chemistry and biology of reactive oxygen species in signaling or stress responses. Nat Chem Biol. 2011;7(8):504–11.

35. Lee D, Khaja S, Velasquez-Castano JC, Dasari M, Sun C, Petros J, Taylor WR, Murthy N. In vivo imaging of hydrogen peroxide with chemiluminescent nanoparticles. Nat Mater. 2007;6(10):765–9.

36. Hu T, He N, Yang Y, Yin C, Sang N, Yang Q. DEC2 expression is positively correlated with HIF-1 activation and the invasiveness of human osteosarcomas. J Exp Clin Cancer Res. 2015;34(1):22.

37. Wang X, Dong J, Jia L, Zhao T, Lang M, Li Z, Lan C, Li X, Hao J, Wang H, Qin T, Huang C, Yang S, Yu M, Ren H. HIF-2-dependent expression of stem cell factor promotes metastasis in hepatocellular carcinoma. Cancer Lett. 2017;393:113–24.

38. Joseph JP, Harishankar MK, Pillai AA, Devi A. Hypoxia induced EMT: a review on the mechanism of tumor progression and metastasis in OSCC. Oral Oncol. 2018;80:23–32.

39. Rankin EB, Giaccia AJ. Hypoxic control of metastasis. Science. 2016;352(6282):175–80.

40. Jahanban-Esfahlan R, de la Guardia M, Ahmadi D, Yousefi B. Modulating tumor hypoxia by nanomedicine for effective cancer therapy. J Cell Physiol. 2018;233(3):2019–31.

41. Bosco MC, Orazi GD, Del D, Bufalo. Correction to: targeting hypoxia in tumor: a new promising therapeutic strategy. J Exp Clin Cancer Res. 2020;39(1):43.

42. Nohales-Córcoles M, Sevillano-Almerich G, Di Emidio G, Tatone C, Cobo AC, Dumollard R. De Los Santos Molina, Impact of vitrification on the mitochondrial activity and redox homeostasis of human oocyte. Hum Reprod. 2016;31(8):1850–8.

43. Zhang C, Huang H, Chen J, Zuo T, Ou Q, Ruan G, He J, Ding C. DNA supramolecular hydrogel-enabled sustained delivery of metformin for relieving osteoarthritis. ACS Appl Mater Interfaces. 2023;15(13):16369–79.

44. Zhu X-j, Shi Y, Peng J, Guo C-s, Shan N-n, Qin P, Ji X-b, Hou M. The effects of BAFF and BAFF-R-Fc fusion protein in immune thrombocytopenia. Blood. 2009;114(26):5362–7.

45. Zhou J, Wang G, Chen Y, Wang H, Hua Y, Cai Z. Immunogenic cell death in cancer therapy: Present and emerging inducers. J Cell Mol Med. 2019;23(8):4854–65.

46. Ding B, Zheng P, Jiang F, Zhao Y, Wang M, Chang M, Ma Pa, Lin J. MnO$_x$ Nanospikes as nanoadjuvants and immunogenic cell death drugs with enhanced antitumor immunity and antimetastatic effect. Angew Chem. 2020;59(38):16381–4.

47. Wu D, Wang S, Yu G, Chen X. Cell death mediated by the pyroptosis pathway with the aid of nanotechnology: prospects for cancer therapy. Angew Chem. 2021;60(15):8018–34.

48. Ploetz E, Zimpel A, Cauda V, Bauer D, Lamb DC, Haisch C, Zahler S, Vollmar AM, Wuttke S, Engelke H. Metal-Organic Framework nanoparticles induce pyroptosis in cells controlled by the Extracellular pH. Adv Mater (Deerfield Beach Fla). 2020;32(19):e1907267.

49. Xu C, Jiang Y, Han Y, Pu K, Zhang R. A polymer multicellular nanoengager for synergistic NIR-II Photothermal Immunotherapy. Adv Mater. 2021;33(14):e2008061.

Publisher's note